

Evolution of coherent structures in a two-dimensional impinging jet

S. Pieris, X. Zhang, S. Yarusevych*, S. D. Peterson

Department of Mechanical and Mechatronics Engineering
University of Waterloo
200 University Ave. W, Waterloo, Ontario, Canada, N2L 3G1
*syarus@uwaterloo.ca

ABSTRACT

This paper reports the results of an experimental investigation of a normally impinging slot jet created by a nozzle of high aspect ratio. Time resolved planar particle image velocimetry is used to characterize the jet development at Reynolds numbers of 3000 and 6000, with a nozzle-to-plate distance of 4 nozzle widths. Primary vortices form due to the Kelvin-Helmholtz instability in the jet shear layer prior to flow impingement. Frequency and spatial energy distributions of the coherent structures are analyzed. The primary vortices are shed at a Strouhal number of 0.5, and are convected downstream at a velocity of 50% and 62% of the jet centerline velocity for Reynolds numbers of 3000 and 6000, respectively. Vortex merging occurs in the vicinity of the impingement zone. Secondary vortices form at a quarter of the primary vortex shedding frequency, originating from the interaction between the merged primary vortices and the wall.

INTRODUCTION

Impinging jets are encountered in various engineering applications, particularly where relatively high rates of heat and/or mass transfer from a surface are required. Consequently, these flows have been investigated extensively, with previous studies focusing primarily on the thermo-fluids aspects of the flow (e.g., Martin & Buchlin, 2011; Kristiawan *et al.*, 2012; Ianiro *et al.*, 2012). In comparison, fewer investigations have given detailed attention to the development of turbulent coherent structures in impinging jets that have been shown to play a key role in transport processes (O'Donovan & Murray, 2007).

In impinging jet flows, vortical structures form in the shear layers due to the Kelvin-Helmholtz (K-H) instability. The characteristic Strouhal number (St) of these structures has been shown to depend on the flow conditions at the jet exit (Reynolds number and spectrum of fluctuations at the jet exit) and the jet configuration (e.g., nozzle geometry and distance between the nozzle exit and the wall). Thus, a range of Strouhal numbers have been reported in the literature, as summarized by Hadžiabdić & Hanjalić (2008). The K-H vortices enhance the entrainment of ambient air into the main stream, particularly within the impingement zone, and break down in the wall jet region.

The majority of the previous investigations have focused on round impinging jets. In contrast, far fewer studies have considered the two-dimensional jet configuration. Furthermore, exploration of the complex spatio-temporal dynamics of these flows is only enabled by recent advancements in time-resolved velocity field measurements. Notably, Violato *et al.* (2012) and Sodjavi *et al.* (2016) have captured the flow field of both round and chevron-shaped impinging jets using time-resolved tomographic (TR-TOMO) particle image velocimetry (PIV). It is also of interest to quantitatively characterize spatio-temporal flow development, in particular the development of coherent structures in a two-dimensional jet because the impingement of these coherent structures on the wall distinguish the

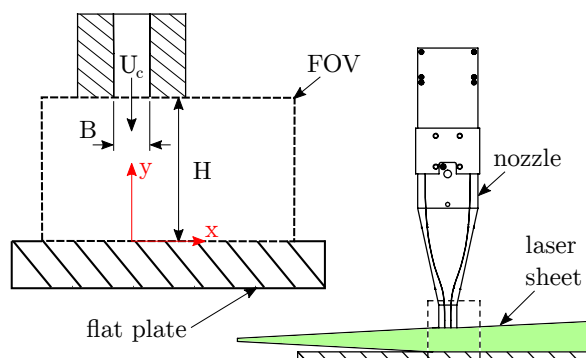


Figure 1: Experimental setup and relevant parameters.

near-wall flow behaviour of the wall jet region from a turbulent wall jet. For instance, unsteady boundary layer separation is triggered by the passage of K-H vortices (Didden & Ho, 1985) affecting the local heat and mass transfer.

The present work studies the formation, evolution, and interaction of the vortical structures in an impinging jet issued from a slot with a large aspect ratio, approximating a two-dimensional jet. Time-resolved planar PIV (2D TR-PIV) is used to capture the instantaneous velocity fields with high spatio-temporal resolution. The results provide insight into the comparability of the vortex dynamics of the two-dimensional jet to that of the axi-symmetric jet, which will facilitate the design of the configurations of plane jet impingement in related engineering scenarios, such as advanced air drying and aircraft de-icing systems.

EXPERIMENTAL METHOD

The impinging jet flow is created using a custom facility constructed at the University of Waterloo. The nozzle used to create the planar impinging jet has a width (B) of 10 mm, a span (L) of 200 mm, and a contraction ratio of 9:1. The jet facility is capable of producing flow velocities up to 30 m s^{-1} in the jet core with mean flow uniformity of 1% across the nozzle exit. The flow is conditioned using a honeycomb and four mesh screens upstream of the contraction. The impingement surface is a black aluminum plate measuring $50B \times 63B$.

Planar TR-PIV is used for measurements. A Photonics DM20-527 Nd-YLF pulsed laser is used for illumination and the flow is seeded with a water-glycol based mixture consisting of droplets with mean diameters of $1 \mu\text{m}$. The laser sheet is projected across the mid-span of the jet exit with a thickness of approximately 1 mm. Figure 1 shows a schematic of the nozzle, plate, and laser sheet arrangement, along with the field of view (FOV) of interest. Particle images are captured using two Photron SA4 high-speed cameras with sensor sizes of $1024 \times 1024 \text{ px}^2$. Each camera is

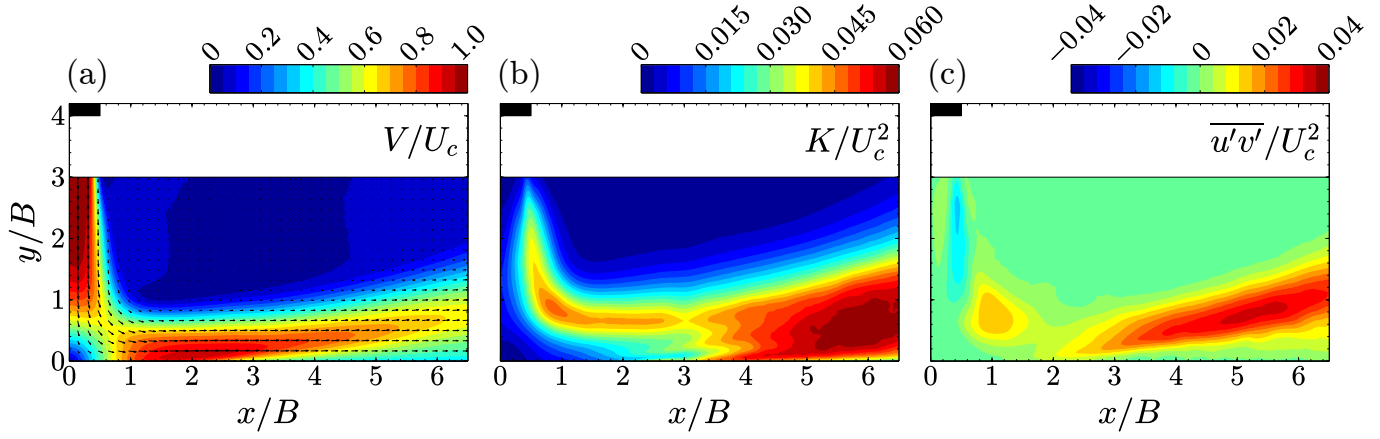


Figure 2: Contours of (a) mean velocity magnitude, (b) turbulent kinetic energy, and (c) Reynolds shear stress for $Re = 3000$. The nozzle exit is shown in black.

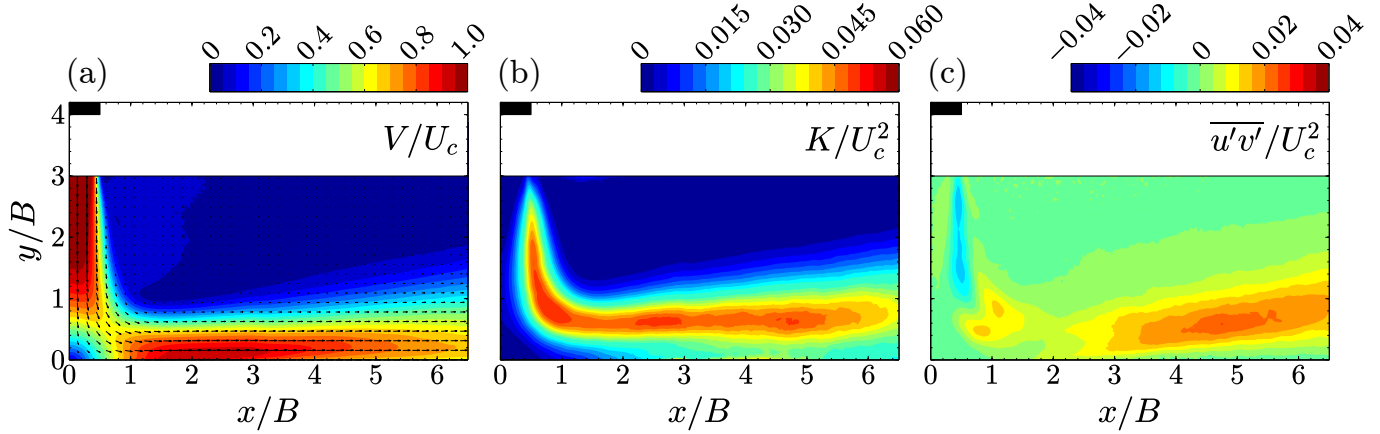


Figure 3: Contours of (a) mean velocity magnitude, (b) turbulent kinetic energy, and (c) Reynolds shear stress for $Re = 6000$. The nozzle exit is shown in black.

equipped with a 105 mm lens with a numerical aperture of $f_{\#} = 2.8$ and a magnification factor of $M = 0.32$, to image a combined FOV of $75 \times 40 \text{ mm}^2$. Each camera sensor is cropped to $640 \times 640 \text{ px}^2$ corresponding to a FOV of $40 \times 40 \text{ mm}^2$ per camera. Particle images are acquired in double frame mode at a frequency of 125 Hz to achieve statistical convergence of time-averaged properties and 3200 Hz for high temporal resolution.

The illumination and imaging systems are synchronized using a LaVision High Speed Controller and DaVis 8 software, with the latter also being used for image processing. The particle images are processed using a multi-pass, sequential cross correlation algorithm in DaVis 8 to calculate velocity vector fields. The final interrogation window is $16 \times 16 \text{ px}^2$ with 75% overlap, resulting in a vector pitch of 0.25 mm.

RESULTS

In the present study, jets at Reynolds numbers ($Re = U_c B / \nu$) 3000 and 6000 impinging on a plate at a nozzle-to-plate spacing (H/B) of 4 are investigated. Figures 2 and 3 show non-dimensionalized mean velocity magnitude (V/U_c), turbulent kinetic energy (K/U_c^2) and Reynolds shear stress ($\overline{u'v'}/U_c^2$) contours for $Re = 3000$ and 6000, respectively. In both cases, significant deceleration of the flow is observed at $y/B \approx 1$, where the shear layers are deflected outward around the stagnation region. This region is characterized by both low velocity magnitude and fluctuations,

and extends up to $x/B \approx 0.5$ and $y/B \approx 0.5$. As the jet develops downstream of the nozzle, amplification of the velocity fluctuations takes place in the shear layers, reaching a maximum at $x/B \approx 1$ and $y/B \approx 1$. This is attributed to the development of primary vortices (PV) driven by the K-H instability in the jet shear layer. A higher magnitude in the velocity fluctuations observed for $Re = 6000$ indicates a higher energy content in the vortical structures, which in turn enhances the momentum flux in the mixing layer (Medina *et al.*, 2013).

The wall jet region originates at $x/B \approx 1$, with a reoriented potential core of high velocity magnitude. Notable differences are observed in the wall jet between the two Reynolds numbers. For $Re = 3000$, deceleration of the fluid in the potential core starts at $x/B \approx 3$, with high turbulent kinetic energy (TKE) distributed across the entire jet region, and the jet is deflected away from the surface. In contrast, for $Re = 6000$, the TKE is more concentrated along the outer shear layer, and the wall jet core remains nearly parallel to the surface.

The results indicate that turbulence is produced in the shear layers of the jet prior to impingement and within the wall jet (figs. 2c and 3c). As the Reynolds number increases, the Reynolds shear stress increases in the free jet shear layer while decreasing in the wall jet shear layer. Generally, low magnitude values are observed in the shear layer of the free jet (negative) and above the stagnation region (positive) prior to the wall jet. A minimum of

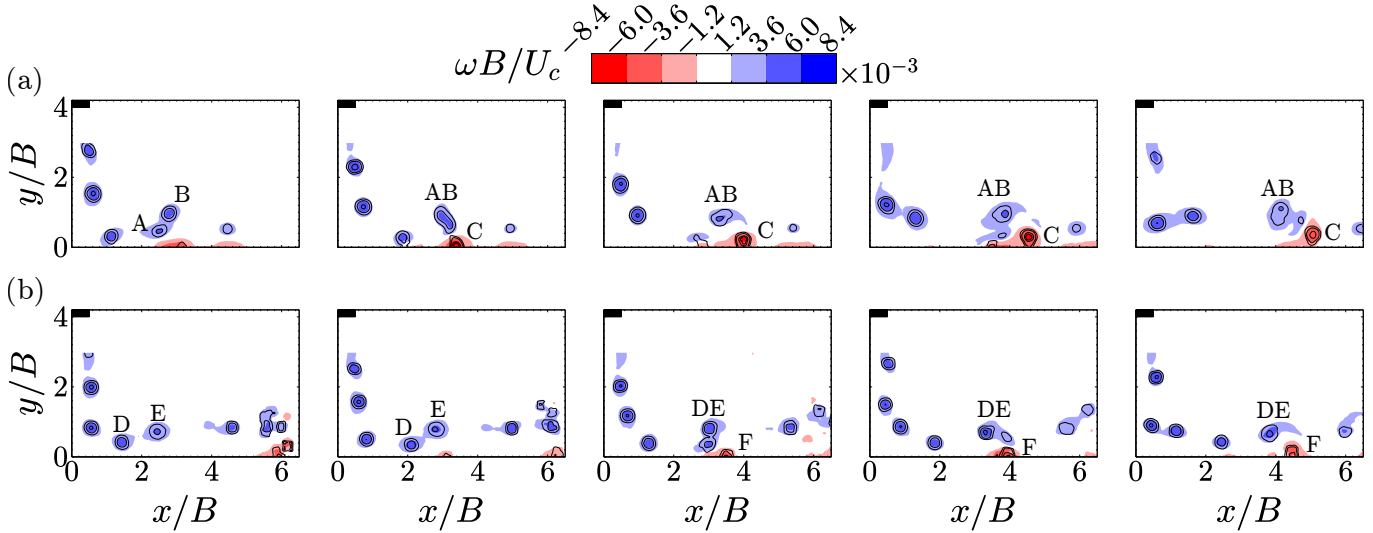


Figure 4: Instantaneous vorticity contours overlaid with λ_2 criterion contours for (a) $Re = 3000$ and (b) $Re = 6000$. Each consecutive image is separated by (a) $t^* = 0.13$ and (b) $t^* = 0.15$. The nozzle exit is shown in black.

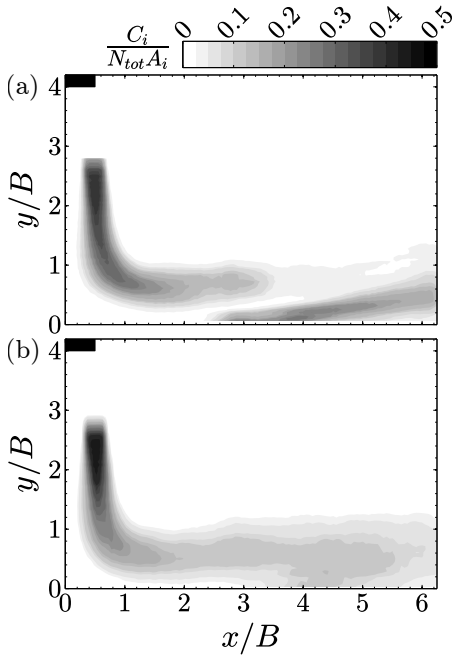


Figure 5: Probability density distribution of vortices identified using λ_2 criterion for (a) $Re = 3000$ and (b) $Re = 6000$. C_i is the number of vortices in each bin, A_i is the bin area, and N_{tot} is the total number of vortices identified. The nozzle exit is shown in black.

$\overline{u'v'}/U_c^2 = -0.01$ is observed, located in the shear layers of the jet prior to impingement for both Reynolds numbers. A maximum in the Reynolds shear stress is observed in the wall jet shear layer at $x/B \approx 5$ and $y/B \approx 0.5$ for both $Re = 3000$ and 6000 , with values of 0.04 and 0.024 , respectively. Combined with the opposing sign of the mean velocity gradient, turbulent production is expected to be weak in the shear layers just downstream of the nozzle and intensify in the shear layers of the wall jet region.

The spatio-temporal development of the coherent structures is illustrated in fig. 4 using a time sequence of vorticity and λ_2 criterion contours (Jeong & Hussain, 1995). The time separation be-

tween each consecutive image is $t^* = tu_c/H = 0.13$ and 0.15 for $Re = 3000$ and 6000 , respectively, where u_c is the average vortex convective velocity in the jet prior to impingement. Primary vortices are formed in the shear layers of the jet due to K-H instabilities directly downstream of the jet exit and are then convected downstream. The shedding of the PVs is expected to shift upstream with an increase in Re due to the growth of the K-H instability. A minor shift of vortex formation is observed, with vortices shedding at $y/B \approx 2$ and 2.5 for $Re = 3000$ and 6000 , respectively. The vortex shedding is characterized by an increase in the velocity fluctuations as seen in figs. 2 and 3. The shedding frequency for both Re is $St \approx 0.5$, while u_c increases from $0.5U_c$ to $0.62U_c$ with an increase in Re , which agrees with the convective velocities reported by Didden & Ho (1985). The passing of the PVs in the wall jet region induces the formation of secondary vortices (SV), at the impingement surface. The formation process is attributed to the strong pressure gradients caused by the passage of PVs, which decelerates a thin layer of fluid near the wall that subsequently rolls up to form coherent structures (Hadžiabdić & Hanjalić, 2008). This SV formation has been reported in several previous studies for both round and slot jets (e.g., El Hassan *et al.*, 2012; Tummers *et al.*, 2011; Didden & Ho, 1985).

Figure 4a shows a shedding cycle of a SV (labelled C) and the passing of two PVs (labelled A and B) for $Re = 3000$. Vortices A and B begin to merge at $x/B \approx 3$, in the wall jet region, where vortex C of opposite vorticity forms at the surface. As vortices A and B complete merging, vortex C is formed at the wall, producing a vortex pair with the merged vortex AB. Vortices AB and C convect downstream and move away from the surface. The formation and development of the vortex pair correspond with the low velocity magnitude and high velocity fluctuation peak seen in figs. 2a and 2b, respectively. The SV formation process is less pronounced for $Re = 6000$. As PVs labelled D and E merge, a comparatively smaller SV, labelled F, is observed. The merged vortex DE and F convect parallel to the surface. The deflection away from the surface observed for $Re = 3000$ is not observed for $Re = 6000$, as the core of the wall jet is more energetic and reduces the deflection of the SV. In the first frame of fig. 4b, a PV and SV pair break down in the region $x/B > 5.5$. This vortex breakdown process corresponds to the high magnitude in the mean velocity and low magnitude in the velocity fluctuations in the region of SV formation for $Re = 6000$. Further-

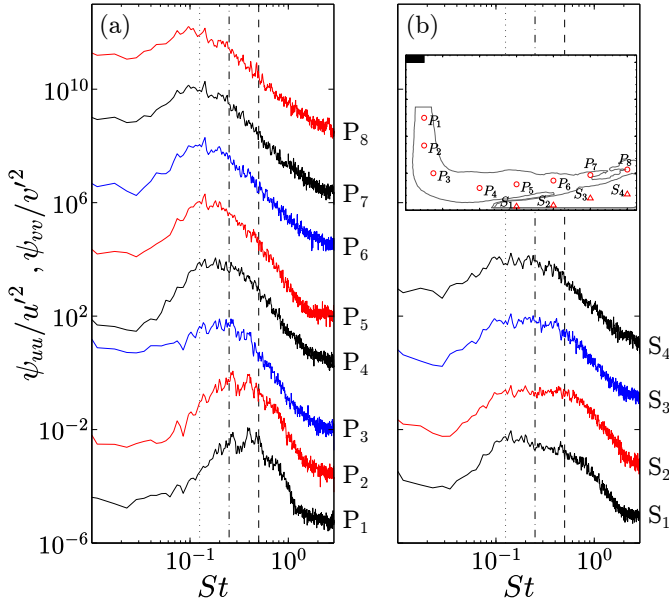


Figure 6: Frequency spectra of stream normal fluctuating velocity for $Re = 3000$ at several locations along (a) primary vortex trajectory and (b) secondary vortex trajectory shown in the inset image. Each spectrum is stepped by two orders of magnitude. Vertical lines correspond to $St = 0.5$ (—), $St = 0.25$ (-·-) and $St = 0.125$ (···).

more, beyond $x/B = 5$, the decrease in the two-dimensional velocity fluctuations indicates transition to a turbulent regime, where the flow is essentially three-dimensional.

Figure 5 shows the probability density distribution (PDD) of vortex core locations obtained via a λ_2 criterion based vortex identification routine. For both Re , a peak in the PDD is observed around $x/B = 0.5$ and $y/B = 2.5$ indicating the localized PV formation in the shear layers of the jet. In comparison with the $Re = 3000$ case, for $Re = 6000$ the PVs penetrate further through the jet core towards the wall since the large eddies in the jet shear layer are more energetic at higher Reynolds numbers; this is corroborated by the larger TKE values in the jet shear layer. The flow at $Re = 3000$ presents a distinct bi-modal distribution in vortex trajectories for $x/B > 2.2$, with one near-wall peak and another peak located in the shear layer of the wall jet region. The latter remains discernible until $x/B \approx 5$. The bimodal distribution of vortices initiates at $x/B \approx 2.5$, directly upstream of the location where the a significant increase in TKE is observed (fig. 2b). At $x/B \approx 3$, local maxima in TKE are observed in three distinct transverse locations, $y/B \approx 0.7, 0.3$ and 0 , respectively, attributed to the shedding and growth of SVs due to the passage of PVs. This bi-modal distribution is not observed for $Re = 6000$, indicating a quicker decay in jet potential core and an earlier onset of a turbulent wall jet, resulting from the strong mixing of more energetic large eddies in flows at this higher Reynolds number.

The evolution of the coherent structures is analyzed using power spectra of velocity fluctuation presented in figs. 6 and 7 for $Re = 3000$ and 6000 , respectively. The spectra were computed using Welch's method (Welch, 1967) and pertain to several locations along the trajectories of PV and SV, indicated in figure insets as points P and S, respectively. Figure 6a features broad peaks for P_1 centred at approximately $St = 0.44$. As the flow develops downstream, a subharmonic growth is observed at $St \approx 0.27$, attributed to periodic vortex merging. Figure 6b features a broad energy content between $0.1 < St < 0.95$, reflecting velocity fluctuations induced by

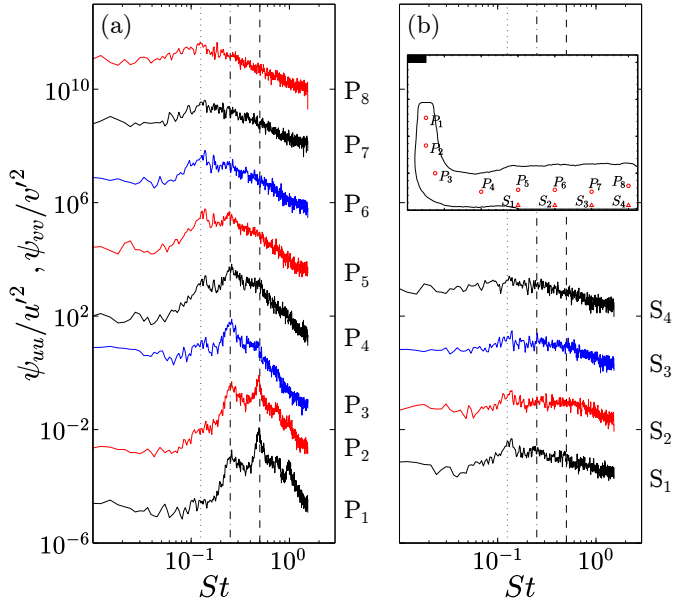


Figure 7: Frequency spectra of stream normal fluctuating velocity for $Re = 6000$ at several locations along (a) primary vortex trajectory and (b) secondary vortex trajectory shown in the inset image. Each spectrum is stepped by two orders of magnitude. Vertical lines correspond to $St = 0.5$ (—), $St = 0.25$ (-·-) and $St = 0.125$ (···).

both PV and SV structures in the near-wall region.

For $Re = 6000$, more narrow peaks are observed in the power spectra at P_1 centred at $St = 0.5$ and 0.25 (fig. 7a) indicating lower cycle-to-cycle variations in vortex shedding and merging compared to those for $Re = 3000$. The earlier emergence of the subharmonic peak is attributed to the earlier onset of vortex merging produced due to the earlier shear layer roll-up expected for the higher Re . As the flow develops downstream, the subharmonic energy content increases, while that of the fundamental frequency decays. Eventually, a broad energy distribution is observed for P_7 and P_8 , similar to the spectra of developing turbulent shear flows. This indicates earlier vortex breakdown for $Re = 6000$ compared to that for $Re = 3000$, which is expected for the higher Reynolds number and is consistent with the observation from instantaneous vorticity sequence (fig. 4) and PDD (fig. 5). Comparing the spectra pertaining to the near wall region (figs. 6b and 7b) shows that the energy distribution is more broadband for $Re = 6000$ with a slight peak observed at $St = 0.125$, indicating that the formation of the SV has a characteristic frequency equal to the second subharmonic of the PV formation frequency.

Figures 8 and 9 show the spatial distribution of the fluctuating velocity components u and v , respectively, pertaining to specific frequency bands of interest. Velocity fluctuations are filtered using a centred bandwidth of $St = 0.02$ at $St = 0.5, 0.25$ and 0.125 . The u -component of velocity fluctuations related to the frequency peak $St = 0.5$ is localized in the shear layers of the jet prior to impingement. The maxima in u -component of velocity fluctuations related to this frequency is located at $x/B \approx 0.5$ and $y/B \approx 2.5$, which corresponds to the location of PV formation observed in instantaneous vorticity fields. At $St = 0.5$, the v -component fluctuations are distributed over a larger area near the flow reorientation region encompassing the stagnation zone and in the wall jet region; however, the magnitude of these fluctuations are relatively small since the passage of PVs causes larger velocity fluctuations normal to the direction of vortex propagation.

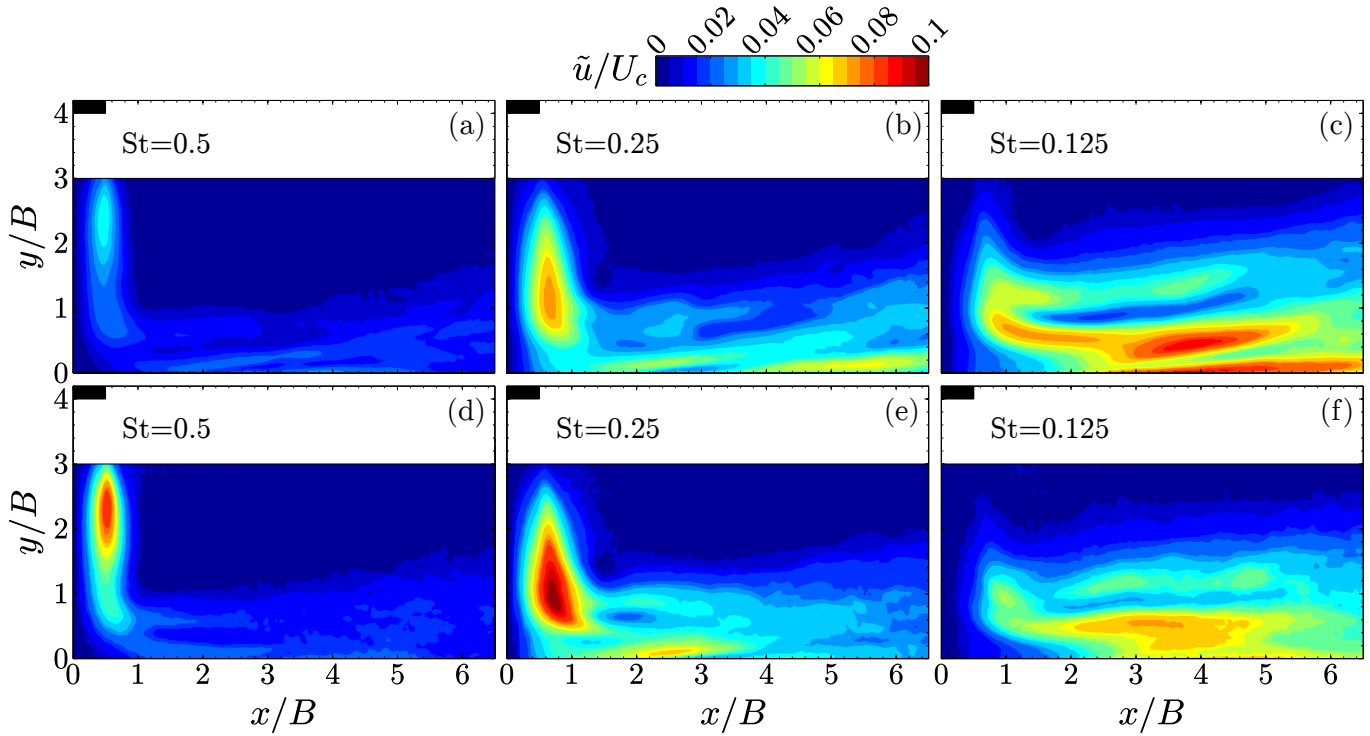


Figure 8: Band-pass spectral energy contours of fluctuating u -component velocity (a-c) $Re = 3000$ and (d-f) $Re = 6000$ centred at $St = 0.5, 0.25$ and 0.125 using a band width of $St = \pm 0.01$.

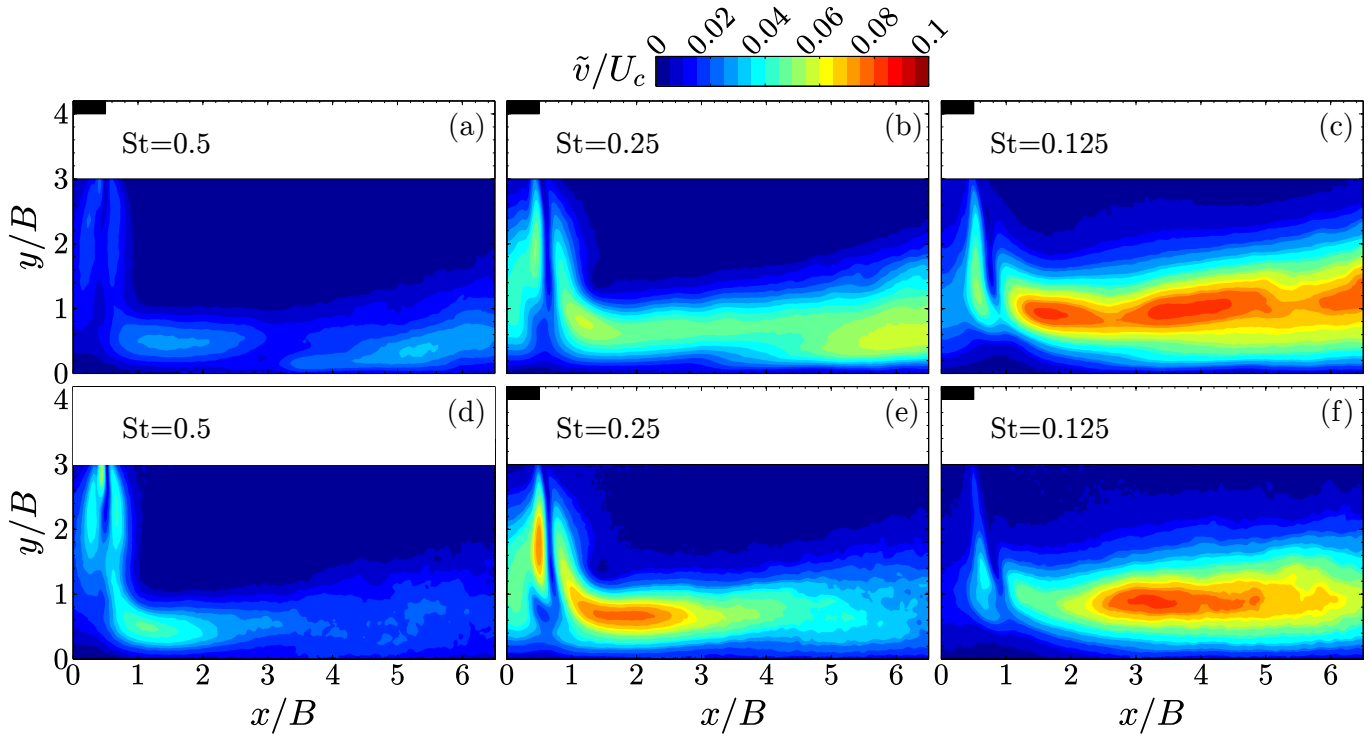


Figure 9: Band-pass spectral energy contours of fluctuating v -component velocity (a-c) $Re = 3000$ and (d-f) $Re = 6000$ centred at $St = 0.5, 0.25$ and 0.125 using a band width of $St = \pm 0.01$.

The u -component fluctuations filtered at $St = 0.25$ are widely distributed over the shear layer prior to impingements with peak fluctuations at $x/B = 0.75$ and $y/B = 1$. Comparatively, the v -component fluctuations are distributed mainly in the shear layer of the wall jet region ($x/B > 1$), being associated with vortex merging. The extension of v -component fluctuations into the jet core prior

to impingement at this frequency band infers the interaction of the merging events and upstream vortex formation.

The energy content distribution at $St = 0.125$ reflects secondary vortex formation in the u -component fluctuations (figs. 8c and 8f). For $Re = 3000$, the peaks in the fluctuations are observed in both the wall jet shear layer and in the near wall region beyond

$x/B > 3$, confirming the bimodal trajectories observed in the probability density distribution. In contrast, for $Re = 6000$, the fluctuations associated with $St = 0.125$ are less localized and the magnitude is lower in the near wall region, indicating that the SVs are less coherent. Beyond $x/B = 5$, the PVs and SVs for both Reynolds numbers undergo breakdown, as characterized by the sharp drop in the energy content of band filtered two-dimensional velocity fluctuations.

The spatial distribution of band-pass filtered frequency content shows notable spatial overlaps of the three frequency bands, implying the interaction between the downstream merging events and upstream vortex formation. A feedback loop was suggested by Ho & Nosseir (1981) and Didden & Ho (1985), where the pressure fluctuations produced due to formation of the SV at the wall propagate upstream, affecting the PV formation in the shear layers prior to impingement.

CONCLUSIONS

Coherent structures in a normally impinging, high aspect ratio slot jet are captured using time resolved planar particle image velocimetry for $Re = 3000$ and 6000 , and a nozzle-to-plate spacing of $H/B = 4$. Instantaneous vorticity fields show the formation of primary Kelvin-Helmholtz vortices in the shear layers of the jet prior to impingement, which are convected downstream. The primary vortices merge and interact with the impingement surface in the wall jet region, inducing the roll-up and shedding of secondary vortices. The behaviour of secondary vortices is dependent on the Reynolds number, with more coherent secondary vortex shedding observed at the lower Reynolds number. The shedding frequency of the primary vortex was found to be $St = 0.5$ for both Reynolds numbers, with a more distinct peak observed in the velocity fluctuation spectra for a Reynolds number of 6000 . The secondary vortex shedding frequency was found to be a quarter of the primary vortex shedding frequency. The analysis of spatial distribution of the energy content associated with the characteristic frequencies of the detected coherent structures revealed that the energy content of the velocity fluctuations associated with the formation of primary vortices is localized in the shear layers of the free jet. The energy content at other frequency bands overlap spatially. This suggests that secondary vortex formation affects the flow upstream of the stagnation region.

ACKNOWLEDGEMENT

The authors gratefully acknowledge the Natural Sciences and Engineering Research Council of Canada (NSERC), Ontario Centres of Excellence, and Suncor Energy for funding this work.

REFERENCES

Didden, N. & Ho, C. M. 1985 Unsteady separation in a boundary layer produced by an impinging jet. *Journal of Fluid Mechanics*

160, 235–256.

- El Hassan, M., Assoum, H. H., Sobolik, V., Vétel, J., Abed-Meraim, K., Garon, A. & Sakout, A. 2012 Experimental investigation of the wall shear stress and the vortex dynamics in a circular impinging jet. *Experiments in Fluids* **52** (6), 1475–1489.
- Hadžiabdić, M. & Hanjalić, K. 2008 Vortical structures and heat transfer in a round impinging jet. *Journal of Fluid Mechanics* **596** (2008), 221–260.
- Ho, C. M. & Nosseir, N. S. 1981 Dynamics of an impinging jet. Part 1. The feedback phenomenon. *Journal of Fluid Mechanics* **105** (-1), 119.
- Ianiro, A., Violato, D., Scarano, F. & Cardone, G. 2012 Three dimensional features in swirling impinging jets. *15th International Symposium on Flow Visualization*.
- Jeong, J. & Hussain, F. 1995 On the identification of a vortex. *Journal of Fluid Mechanics* **285**, 69.
- Kristiawan, M., Meslem, A., Nastase, I. & Sobolik, V. 2012 Wall shear rates and mass transfer in impinging jets: Comparison of circular convergent and cross-shaped orifice nozzles. *International Journal of Heat and Mass Transfer* **55** (1-3), 282–293.
- Martin, R. H. & Buchlin, J. 2011 Jet impingement heat transfer from lobed nozzles. *International Journal of Thermal Sciences* **50** (7), 1199–1206.
- Medina, H., Benard, E. & Early, J. M. 2013 Reynolds Number Effects on Fully Developed Pulsed Jets Impinging on Flat Surfaces. *AIAA Journal* **51** (June), 1–14.
- O'Donovan, T. S. & Murray, D. B. 2007 Jet impingement heat transfer - Part II: A temporal investigation of heat transfer and local fluid velocities. *International Journal of Heat and Mass Transfer* **50** (17-18), 3302–3314.
- Sodjavi, K., Montagné, B., Bragança, P., Meslem, A., Byrne, P., Degouet, C. & Sobolik, V. 2016 PIV and electrodiffusion diagnostics of flow field, wall shear stress and mass transfer beneath three round submerged impinging jets. *Experimental Thermal and Fluid Science* **70**, 417–436.
- Tummers, M. J., Jacobse, J. & Voorbrood, S. G. J. 2011 Turbulent flow in the near field of a round impinging jet. *International Journal of Heat and Mass Transfer* **54** (23-24), 4939–4948.
- Violato, D., Ianiro, A., Cardone, G. & Scarano, F. 2012 Three-dimensional vortex dynamics and convective heat transfer in circular and chevron impinging jets. *International Journal of Heat and Fluid Flow* **37**, 22–36.
- Welch, P. D. 1967 The use of fast Fourier transform for the estimation of power spectra: A method based on time averaging over short, modified periodograms. *IEEE Transactions on audio and electroacoustics* **15** (2), 70–73.